Persistent Fe moments in the normal-state collapsed-tetragonal phase of the pressure-induced superconductor $Ca_{0.67}Sr_{0.33}Fe_2As_2$

J. R. Jeffries,[1] N. P. Butch,[1,2] M. J. Lipp,[1] J. A. Bradley,[1] K. Kirshenbaum,[3] S. R. Saha,[3] J. Paglione,[3] C. Kenney-Benson,[4] Y. Xiao,[4] P. Chow,[4] and W. J. Evans[1]

[1]*Condensed Matter and Materials Division, Lawrence Livermore National Laboratory, Livermore, California 94550, USA*
[2]*NIST Center for Neutron Research, National Institute of Standards and Technology, Gaithersburg, Maryland 20899, USA*
[3]*Center for Nanophysics and Advanced Materials, Department of Physics, University of Maryland, College Park, Maryland 20742, USA*
[4]*HP-CAT, Geophysical Laboratory, Carnegie Institute of Washington, Argonne, Illinois 60439, USA*

Using nonresonant Fe $K\beta$ x-ray emission spectroscopy, we reveal that Sr substitution into $CaFe_2As_2$ decouples the Fe moment from the volume collapse transition, yielding a collapsed-tetragonal, paramagnetic normal state out of which superconductivity develops. X-ray diffraction measurements implicate the c-axis lattice parameter as the controlling criterion for the Fe moment, promoting a generic description for the appearance of pressure-induced superconductivity in the alkaline-earth-based 122 ferropnictides (AFe_2As_2). The evolution of T_c with pressure lends support to theories for superconductivity involving unconventional pairing mediated by magnetic fluctuations.

PACS number(s): 74.62.Fj, 74.70.Xa, 75.20.Hr, 78.70.En

I. INTRODUCTION

Early in the research on iron pnictide superconductors, theoretical calculations strongly suggested that conventional, phonon-mediated superconductivity was incompatible with observed critical temperatures T_c [1–4]. Additionally, several systems have shown an empirical correlation between T_c and the structural parameters [5–7]. Since then, iron-based superconductors have proven a fertile playground for understanding how structural and magnetic degrees of freedom affect superconductivity [8–11]. While there are no fewer than five systems sharing similar structural building blocks, the most widely studied ferropnictide superconductors are those that crystallize in the tetragonal $ThCr_2Si_2$ crystal structure. The so-named "122" compounds have the chemical formula AFe_2X_2 (where A is an alkaline-earth element, an alkali metal, or Eu and X is a pnictogen atom), exhibit antiferromagnetic order at ambient pressure, and are amenable to a variety of chemical substitutions that suppress magnetism and induce superconductivity [8,9,11–14].

With applied pressure or suitable chemical substitution, the parent 122 compounds undergo an isostructural volume collapse that is driven by the development of As-As bonding across the mirror plane of the crystal structure [15–19]. This collapsed-tetragonal (CT) phase abruptly cuts off the antiferromagnetic order and, in most cases, supports superconductivity in the vicinity of the truncated magnetic order [20]. The dissenting member of the 122 family, $CaFe_2As_2$, shows no signs of superconductivity in the CT phase when subjected to hydrostatic compression or isovalent P substitution, which mimics pressure through a reduction in the unit cell volume [21,22]. This absence of superconductivity resonates with the scenario determined from neutron scattering measurements where the Fe moments in the CT phase of $CaFe_2As_2$ are quenched [23,24], supporting the strong link between the presence of magnetic fluctuations and the occurrence of superconductivity in this family of compounds [3,4]. However, in Pr- and Nd-doped $CaFe_2As_2$, superconductivity can be induced from a normal state comprising nonmagnetic Fe atoms

[25]. These opposing behaviors with respect to the magnetic state of the Fe atoms question the roles of magnetic and charge fluctuations in inducing superconductivity in the 122 systems.

In order to tune the structural and magnetic degrees of freedom without charge doping, we have performed high-pressure experiments on $Ca_{0.67}Sr_{0.33}Fe_2As_2$, which provides a larger-volume system that decouples the quenching of Fe moments from the volume-collapse transition. Using nonresonant Fe $K\beta$ x-ray emission spectroscopy (XES) and x-ray diffraction (XRD), we report the evolution of the instantaneous Fe moments of $Ca_{0.67}Sr_{0.33}Fe_2As_2$ as a function of pressure and crystal structure. We find that the Fe moments persist into the CT phase, yielding a magnetic normal state out of which superconductivity develops. Consistent with theoretical calculations, the magnitude of the Fe moments appears to be largely controlled by the c-axis lattice parameter, providing a natural mechanism to explain the observed superconductivity in the 122 systems under pressure.

II. EXPERIMENTAL DETAILS

Single crystals of $(Ca_{0.67}Sr_{0.33})Fe_2As_2$ were synthesized with a flux-growth technique previously described [26]. For the XES measurements, small single crystals (11.3-keV data) or powder from the single crystal growth (20-keV data) were loaded into diamond anvil cells (DAC) that employed Be gaskets (~3 mm diameter). For XRD experiments, a powder was loaded into a spring steel gasket. The DAC was pressurized using a gas membrane, and the pressure in the sample chamber was calibrated using the shift of the ruby fluorescence line (XES data) or the lattice parameter of Cu (XRD data). Silicone oil (XES data) or neon (XRD data) were used as the pressure-transmitting media.

The XES measurements were performed at beamline 16-IDD and the XRD measurements at 16-BMD of the High-Pressure Collaborative Access Team (HPCAT) at the Advanced Photon Source. For XES, 11.3- and 20.0-keV, microfocused x-ray beams (approximately 35×50 μm^2)

entered through one of the diamond anvils, while the emitted Fe $K\beta$ x rays were collected after passing through the Be gasket. Fe $K\beta$ spectra were acquired by scanning a bent Si (440) analyzer in 0.25 eV steps; resolution was 1 eV. XRD data were collected in a transmission geometry using a 30 keV, $10 \times 10 \ \mu m^2$ microfocused x-ray beam and a Mar345 image plate. Analysis procedures for the XRD data are identical to Ref. [18]. Additionally, for the 20.0 keV incident energy XES setup, x-ray diffraction was performed *in situ* to confirm the crystal structure of the $Ca_{0.67}Sr_{0.33}Fe_2As_2$ specimen (see the Appendix). Low-temperature XES and XRD measurements were performed in a He-flow cryostat.

III. RESULTS AND DISCUSSION

A. X-ray emission spectroscopy

The Fe $K\beta$ spectra are sensitive, bulk probes of the instantaneous Fe moment due to atomic $3p$-$3d$ orbital overlap. An incoming x ray with an energy greater than the Fe K edge can excite a $1s$ electron from the core of an Fe atom into the continuum, leaving a $1s$ core-hole that can be filled with a decay from the $3p$ shell. This $3p$-$1s$ decay in Fe emits an x ray, the $K\beta$ line, at 7058 eV and leaves a final-state core-hole in the $3p$ level. In the presence of a $3d$ moment, the spin degeneracy of this $3p$ core-hole is lifted, producing an energy difference between the spin states of the $3p$ core-hole, and yielding an emission spectrum with a predominant $K\beta$ peak and a weaker satellite $K\beta'$ peak [27,28]. For small-moment systems, like $Ca_{0.67}Sr_{0.33}Fe_2As_2$, the $K\beta'$ portion of a spectrum appears as a shoulder, rather than a distinct peak, on the low-energy side of the main $K\beta$ peak. Unfortunately, a low-energy shoulder exists even in nonmagnetic Fe systems [29] and, as such, a systematic analysis of the *entire* emission spectrum is necessary to extract a quantitative Fe moment.

Here we follow the integrated absolute difference (IAD) method to evaluate the Fe moment in $Ca_{0.67}Sr_{0.33}Fe_2As_2$ under pressure [30]. An IAD analysis proceeds as follows: Each spectrum is normalized such that its integral is unity, a unit-normalized reference spectrum is subtracted from each spectra to yield a difference spectrum, and the absolute values of the difference spectra are integrated to yield quantitative IAD values that are proportional to the Fe moment for each spectrum. For tetrahedrally coordinated Fe atoms, the IAD value can be converted to an Fe moment (in μ_B) using the calibration provided by Gretarsson *et al.* [31]. For pressure-dependent measurements we use our room-temperature, 0.1-GPa data as the reference; Fe moment measurements are thus measured relative to that at 0.1 GPa, which is near enough to ambient pressure to use the ambient-pressure value of about 1.1 μ_B for the AFe$_2$As$_2$ systems [31].

Figure 1 shows example, ambient-pressure XES spectra at 298 and 75 K and their difference (a) as well as the extracted Fe moments (b) from these XES measurements. The Fe moment decreases to approximately 0.8 μ_B at 125 K. The data point at 27 K is extrapolated back to ambient pressure from DAC data at that temperature. From room temperature down to 100 K, the temperature-dependent evolution can be described as a line, yielding a slope of approximately 0.001 μ_B/K. Below 100 K, the Fe moment displays a weaker temperature
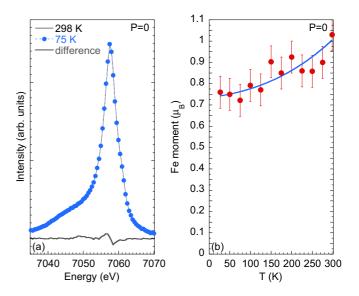

FIG. 1. (Color online) (a) Example, ambient-pressure XES spectra at 298 and 75 K as well as the difference between the two spectra. (b) The Fe moment of $Ca_{0.67}Sr_{0.33}Fe_2As_2$ at ambient pressure as a function of temperature. Error bars are estimated from noise in the spectra to be 0.075 μ_B. The solid line is guide to the eye.

dependence, seeming to saturate at a value near 0.75 μ_B. The entire temperature range presents data consistent with the thermal contraction data of La-doped CaFe$_2$As$_2$ [25]. These data anchor the $P = 0$ portion of the Fe moment contour of Fig. 3(b).

Example room-temperature XES measurements are shown in Figs. 2(a)–2(c), which display the unit-normalized Fe $K\beta$ spectra at 1.5, 3.6, and 6.6 GPa as compared to the spectrum at 0.1 GPa. The shoulder associated with the $K\beta'$ satellite is clearly evident in the low-energy asymmetry of the main peak. The differences between the reference spectrum (0.1-GPa data)
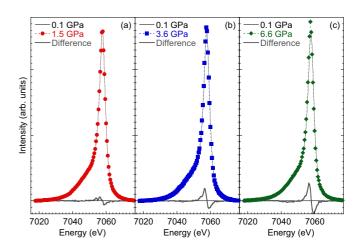

FIG. 2. (Color online) Room-temperature, unit-normalized XES spectra of $(Ca_{0.67}Sr_{0.33})Fe_2As_2$ under pressure (dashed lines, closed symbols) at (a) 1.5, (b) 3.6, and (c) 6.6 GPa as compared with the spectrum at 0.1 GPa (black line, no symbols). The differences between the XES data at each pressure and those at 0.1 GPa are shown as the gray solid lines below the data. Measurement errors due to counting statistics are less than 1%.

and the high-pressure spectra are shown as the solid, gray lines. With increasing pressure, the difference spectra clearly grow larger. The negative dip seen at 6.6 GPa near 7045 eV indicates a loss of spectral weight in the $K\beta'$ satellite portion of the spectrum, implying a reduction in the Fe moment with increasing pressure.

B. Iron moments within the P-T phase diagram

The IAD values from each pressure at 295, 125, and 27 K have been converted to Fe moments, and these values are shown in Fig. 3(a). At each temperature, pressure drives the Fe moment down linearly (within the error of the measurement); the slope of the pressure dependence of the Fe moment, -0.15 μ_B/GPa, is identical within our experimental precision for each temperature. The measured isotherms are overlaid on the phase diagram shown in Fig. 3(b). At 295 K, the
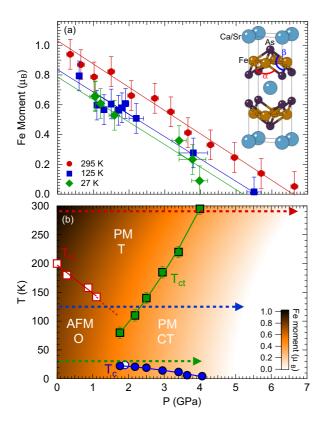

FIG. 3. (Color online) (a) The pressure-dependent Fe moment of $(Ca_{0.67}Sr_{0.33})Fe_2As_2$ at 295, 125, and 27 K; solid lines through the data are linear fits. Horizontal error bars are the larger of 0.1 GPa or the difference between the pressures before and after collection of the spectra. Vertical error bars are 0.1 μ_B estimated from the noise in the spectra. The inset displays the crystal structure of $(Ca_{0.67}Sr_{0.33})Fe_2As_2$, and labels the two As-Fe-As bond angles. (b) The electronic and structural phase diagram of $(Ca_{0.67}Sr_{0.33})Fe_2As_2$, including a contour plot of the Fe moment in μ_B. Open symbols represent data acquired with a pentane:isopentane pressure-transmitting medium, while closed symbols are those with steatite as a pressure-transmitting medium. Error bars are from Ref. [18] and represent transition widths determined from the derivative of the electrical resistivity. The arrows indicate the approximate paths of the XES measurements.

structure of $(Ca_{0.67}Sr_{0.33})Fe_2As_2$ undergoes a tetragonal (T) to collapsed-tetragonal (CT) phase transition near 4 GPa [18]. At 125 K and ambient pressure, $(Ca_{0.67}Sr_{0.33})Fe_2As_2$ is antiferromagnetically ordered (AFM), and the crystal structure is orthorhombic (O) rather than tetragonal. With pressure at 125 K, the system undergoes an O-T transformation that destroys AFM order in favor of a paramagnetic (PM) state near 1.5 GPa; the T-CT phase transition occurs near 2.5 GPa. The Fe moment evolves relatively smoothly through each of these structural/magnetic phase transitions, which have been confirmed via x-ray diffraction (see the Appendix).

In addition to the phase boundaries of Fig. 3(b), a contour plot of the Fe moment in T-P space is included, smoothly interpolating between the three isotherms. At low pressures and intermediate temperatures, the CT phase abruptly destroys the ordered AFM state, but the Fe moment evolves continuously through this transition. This persistence of the Fe moment into the CT phase implies that the destruction of AFM order is not precipitated by the quenching of the local moments. Rather, a more favorable scenario would likely be one where the CT phase supports enhanced spin fluctuations or alters coupling strengths that lead to the destruction of magnetic order [10].

At 1.8 GPa, the moment is about 0.5 μ_B at 27 K, just above the value of $T_c \approx 22$ K determined previously using a steatite pressure-transmitting medium [18]. A measurement of the superconducting transition in pentane:isopentane (see the Appendix) reveals $T_c = 24$ K at 1.9 GPa. This weak dependence on pressure-transmitting media is in contrast to measurements made on pure $SrFe_2As_2$, where different media and high-pressure apparatuses can shift phase boundaries by about 1 GPa (from a starting pressure near 4–5 GPa) [32,33]. The differences between $SrFe_2As_2$ and $(Ca_{0.67}Sr_{0.33})Fe_2As_2$ probably lie in the magnitude of the nonhydrostatic conditions, with the latter possessing small gradients even in solid steatite due to the low pressures where superconductivity is observed. With increasing pressure, the linear suppression of the Fe moment is mirrored by the nearly linear suppression of superconductivity, with T_c disappearing within about 1 GPa of the pressure at which the Fe moment is expected to quench. These observations suggest that the superconducting state of $(Ca_{0.67}Sr_{0.33})Fe_2As_2$ not only develops out of a magnetic normal state, but also that T_c is closely coupled to the magnitude of the Fe moment. This persistent moment near T_c is comparable to $(Ca_{0.78}La_{0.22})Fe_2As_2$, where an approximately 0.5 μ_B moment is present with $T_c \approx 35$ K [19,25]. The correlation between Fe moment and T_c is consistent with theories that evoke spin fluctuations as the pairing mechanism for superconductivity [4].

C. Correlations between crystal structure and iron moment

Unlike the temperature-dependent moments of Pr- and Nd-doped $CaFe_2As_2$ [25], which discontinuously quench upon entering the CT phase, the Fe moments at 295, 125, and 27 K [Fig. 3(a)] of $(Ca_{0.67}Sr_{0.33})Fe_2As_2$ do not exhibit any large discontinuities upon crossing the T-CT or O-T phase boundaries. While this may at first appear inconsistent, a closer examination of the effect of structure on the Fe moments reveals common behavior.
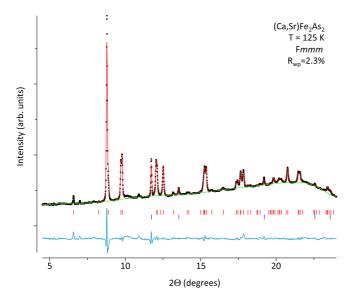
FIG. 4. (Color online) Example refinement of the XRD data at 125 K and $P = 0.9$ GPa. Red tick marks correspond to the orthorhombic ($Fmmm$) phase of $(Ca,Sr)Fe_2As_2$, blue tick marks are from the Cu pressure marker, the background is the green line, the refinement is the red line through the black data points, and the residual of the refinement is the light blue line beneath the pattern.

An example XRD pattern and refinement at $T = 125$ K and $P = 0.9$ GPa are shown in Fig. 4. Information about the crystal structure can be obtained from these XRD patterns, and the pressure at which each pattern is taken can be converted to the Fe moment based on the results of Sec. III B. Figure 5 shows the evolutions of the following structural parameters of $(Ca_{0.67}Sr_{0.33})Fe_2As_2$ at 295 and 125 K as functions of the Fe moment: the orthorhombic (a_O and b_O) and tetragonal (a_T) basal plane lattice parameters; the c-axis lattice parameter; the volume per formula unit ($V/\text{f.u.}$); the As-Fe-As bond angles; as well as the Fe-As bond length (d_{Fe-As}) and the As-As mirror plane spacing (d_{As-As}). The a_T, c, and $V/\text{f.u.}$ parameters show significant overlap at 295 and 125 K, whereas the Fe-As separation and the As-Fe-As bond angles do not. This implies that the lattice parameters, rather than the internal structural degrees of freedom, are the dominant factors controlling the magnitude of the Fe moment in $(Ca_{0.67}Sr_{0.33})Fe_2As_2$. This correlation is consistent with the supposition that structure plays an important role in setting the magnetic energy scales of the AFe_2As_2 systems [34].

Including data from $(Ca_{0.92}Nd_{0.08})Fe_2As_2$ further illuminates the correlations between structure and Fe moment. Figures 5(a) and 5(b) include structure data for $(Ca_{0.92}Nd_{0.08})Fe_2As_2$ taken as a function of temperature [note: $(Ca_{0.78}La_{0.22})Fe_2As_2$ behaves nearly identical] [19,25]. While the T-dependent (and thus Fe-moment-dependent) a-axis lattice parameter of Nd-doped $CaFe_2As_2$ is distinctly different from that of $(Ca_{0.67}Sr_{0.33})Fe_2As_2$ under pressure, the c-axis lattice parameters for these compounds follow strikingly similar behavior as a function of Fe moment. The temperature-induced T-CT transition in $(Ca_{0.92}Nd_{0.08})Fe_2As_2$ results in a large ($\sim 5\%$) change in the c-axis lattice parameter that yields a zero-moment CT phase with $c < 10.65$ Å [25].
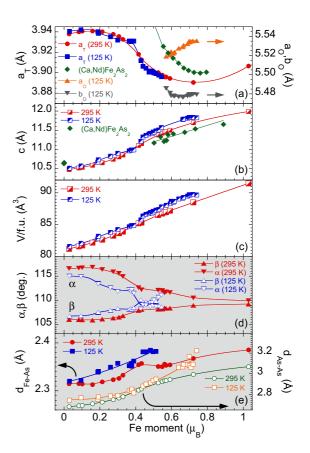

FIG. 5. (Color online) Crystal structure parameters of $(Ca_{0.67}Sr_{0.33})Fe_2As_2$ as a function of Fe moment for different temperatures: (a) a_T, a_O, and b_O, lattice parameters; (b) c lattice parameter; and (c) unit cell volume per formula unit $V/\text{f.u.}$ The internal degrees of freedom of the crystal structure: (d) As-Fe-As bond angles (see inset of Fig. 3), and (e) the Fe-As and As-As bond distances. The a- and c-axis lattice parameters (from temperature-dependent measurements) for $(Ca_{0.92}Nd_{0.08})Fe_2As_2$ are included in (a) and (b), respectively [25]. Error bars for the structure are smaller than the data markers.

In contrast, the T-CT transition in $(Ca_{0.67}Sr_{0.33})Fe_2As_2$ at 300 K results in a 1%–2% change and a c-axis lattice parameter near 10.9 Å. When the c-axis lattice parameter of $(Ca_{0.67}Sr_{0.33})Fe_2As_2$ is compressed to $c < 10.65$ Å at either 300 or 125 K, the Fe moment is quenched. If one assumes a simple linear relationship between the c-axis lattice parameter and the magnitude of the Fe moment, then the T-CT transition in $(Ca_{0.67}Sr_{0.33})Fe_2As_2$ would be expected to generate a reduction in Fe moment of about 0.1 μ_B, which is the size of the error in the XES measurements. Given the magnitude of the T-CT transition and the error in the XES measurements, it is thus not surprising that the measured Fe moment does not show dramatic changes upon passing through the phase boundaries. The strong correlation between the c-axis lattice parameter and the Fe moment is in excellent qualitative agreement with theoretical calculations [3,10,36], but it should be noted that the pressure-dependent volume contraction of $(Ca_{0.67}Sr_{0.33})Fe_2As_2$ is almost entirely driven by the c-axis lattice parameter (the a-axis lattice parameter is actually expanding over a portion of phase space). Therefore,

whether the mechanism for moment loss is driven by changes in the atomic volume of Fe, as suggested for mantle minerals [35], or some *c*-axis-dependent internal coordination remains ambiguous.

IV. CONCLUSIONS

These experimental results challenge the notion that the Fe moment is universally quenched in the CT phase of the 122 systems, and instead promote a generic description of the 122 systems under pressure. With increasing pressure, As-As bonding develops across the mirror plane of the crystal structure, isostructurally collapsing the structure and truncating the AFM state. While the Fe moments in the CT phase of undoped $CaFe_2As_2$ are quenched [23,24], we have shown that the CT phase can in fact support a substantial Fe moment ($\sim 0.5\ \mu_B$) that appears to be strongly coupled to the *c*-axis lattice parameter, which is controlled by the size of the alkaline earth atom, thermal contraction, and the volume change induced by the CT phase. Details of the crystal structure thus govern the magnitude of the Fe moment in the CT phase, potentially providing a paramagnetic normal state out of which superconductivity can develop even in the absence of charge doping. That the pressure-dependent suppression of T_c tracks that of the Fe moment supports the picture of an unconventional superconducting state mediated by magnetic fluctuations. This generic picture suggests that driving the CT phase to ambient pressure while maintaining an Fe moment should be a promising route to high-temperature, magnetically mediated superconductivity in the 122 systems.

ACKNOWLEDGMENTS

APPENDIX

1. Low-temperature XRD and phase boundaries

In an effort to confirm that the phase boundaries were crossed in the XES experiments, XRD measurements were performed using two different experimental setups: (1) an *in situ* configuration where XRD data were acquired in a cryostat along with XES spectra at Sector 16 IDD-D of the Advanced Photon Source, and (2) a configuration optimized for XRD data in a cryostat taken at Sector 16 BM-D at the Advanced
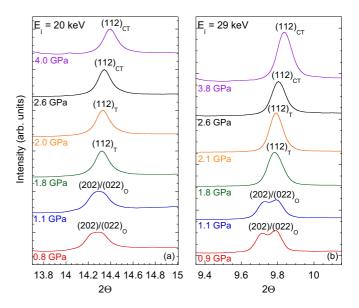

FIG. 6. (Color online) Representative x-ray diffraction acquired at 125 K of the region around the ambient-pressure (202)/(022) orthorhombic Bragg peaks showing their collapse to a single (112) tetragonal Bragg reflection. Configuration 1 is shown in (a) and configuration 2 in (b); both use neon as a pressure-transmitting medium. Subscripts associated with the labeled peaks indicate the structural phase: orthorhombic (O), tetragonal (T), and collapsed tetragonal (CT).

Photon Source. In configuration 1, the XRD patterns were collected on a CCD camera (MarSX165), and an incident beam energy of 20 keV ($\lambda_{inc} = 0.6199$ Å) was used. Based on the experimental geometry, there was physically no room for a larger detector than the CCD camera used. For configuration 2, a larger image plate (Mar345) detector was employed along with a higher energy, 29-keV ($\lambda_{inc} = 0.4246$ Å) incident beam. In both cases, the same diamond anvil cell (DAC) design was used, and the He-flow cryostat was the same in both configurations.

The combination of the DAC and cryostat resulted in a practical 2Θ range from about $4°$ to $22°$. The practical range of 2Θ combined with the detector, experimental geometry, and incident energy of configuration 1 yielded Bragg peaks with slightly broader peak profiles. In addition, the sample-detector distance was chosen to maintain sufficient resolution to distinguish the peak splitting associated with the orthorhombic-tetragonal (O-T) phase transformation. This had the natural consequence of reducing the accessible *d* spacings. As such, the 29-keV XRD data had superior accuracy. Nonetheless, the *in situ* XRD data confirmed the crossing of the phase boundaries in the XES experiments, as evidenced by the coalescence of the orthorhombic d(202)/(022) peaks into a single (112) tetragonal peak near 1.8 GPa (Fig. 6).

2. Pressure conditions and pressure media

The XRD data at 125 K in neon shows the O-T phase boundary near 1.6 GPa, and the tetragonal-collapsed-tetragonal (T-CT) phase boundary near 2.4 GPa (Fig. 6). These phase boundaries are in excellent agreement with those
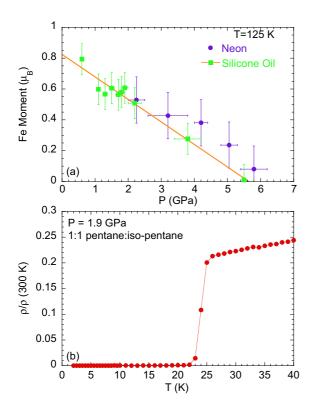
FIG. 7. (Color online) (a) The Fe moment, determined from the IAD analysis of the XES data, as a function of pressure using neon and silicone oil as pressure-transmitting media. (b) Normalized electrical resistivity ρ/ρ (300 K) versus temperature T showing a clear superconducting transition near $T_c = 24$ K in a pentane:isopentane pressure-transmitting medium.

The XES measurements were calibrated with ruby as the pressure marker. The ruby R1 and R2 lines remained well separated throughout the pressure range, suggesting at least quasihydrostatic conditions using both Ne and silicone oil as the pressure-transmitting media. Figure 7(a) illustrates the results of XES measurements at 125 K using both Ne and silicone oil, showing very reasonable agreement between the two pressure media. The silicone oil data are presented in the main text due to its improved error bars. The error bars in the data with the Ne pressure-transmitting medium are larger due to the presence of a spurious As $K\alpha 1$ emission line in the spectra, which enters through the (660) reflection of the Si analyzer. This As emission line is present due to the higher incident energy used for these measurements. The data with silicone oil were acquired with an incident energy below the As K edge, thus removing the As contamination of the spectra.

In addition to these structural phase boundaries, Fig. 3 of the main text contains the electronic phase boundary demarcating superconductivity. Previous results determined this phase boundary using electrical resistivity and a steatite pressure-transmitting medium [18]. Figure 7(b) shows a measurement of the electrical resistivity at 1.9 GPa (the highest pressure achievable in this pressure cell) using a pentane:isopentane pressure-transmitting medium in a hydrostatic, piston-cylinder cell (pressure was calibrated with the superconducting transition of Sn). There is a clear superconducting transition in the sample that occurs at $T_c = 24$ K.

This superconducting transition is included as an open symbol in the superconducting phase boundary presented in Fig. 3 of the main text, and it is in excellent agreement with the boundary determined from measurements with steatite as a pressure-transmitting medium. While this measurement with pentane:isopentane as the pressure-transmitting medium is not truly hydrostatic, it does suggest that the occurrence of superconductivity under pressure in $(Ca_{0.67}Sr_{0.33})Fe_2As_2$ is a relatively robust phenomenon. Measurements at these pressures (>2 GPa) using a truly hydrostatic medium (e.g., helium) are extremely challenging.

All-in-all, the Fe moment, the structural phase boundaries, and the superconducting phase boundary under pressure seem weakly affected by the choice of pressure media between neon, pentane:isopentane, silicone oil, and steatite.

determined from electrical resistivity measurements that used both pentane:isopentane (fluid) and steatite (solid) as pressure-transmitting media [18]. At 125 K, and as determined by electrical resistivity, the O-T phase boundary in pentane:isopentane is about 1.4 GPa, and the T-CT phase boundary in steatite is about 2.3 GPa. These facts would suggest that the structural phase boundaries are, at most, weakly affected by the choice of pressure-transmitting medium.

[1] L. Boeri, O. V. Dolgov, and A. A. Golubov, Phys. Rev. Lett. **101**, 026403 (2008).

[2] I. I. Mazin, D. J. Singh, M. D. Johannes, and M. H. Du, Phys. Rev. Lett. **101**, 057003 (2008).

[3] T. Yildirim, Phys. Rev. Lett. **102**, 037003 (2009).

[4] P. J. Hirschfeld, M. M. Korshunov, and I. I. Mazin, Rep. Prog. Phys. **74**, 124508 (2011).

[5] C.-H. Lee, A. Iyo, H. Eisaki, H. Kito, M. T. Fernandez-Diaz, T. Ito, K. Kihou, H. Matsuhata, M. Braden, and K. Yamada, J. Phys. Soc. Jpn. **77**, 083704 (2008).

[6] J. Zhao, Q. Huang, C. De La Cruz, S. Li, J. W. Lynn, Y. Chen, M. A. Green, G. F. Chen, G. Li, Z. Li, J. L. Luo, N. L. Wang, and P. Dai, Nat. Mater. **7**, 953 (2008).

[7] S. A. J. Kimber, A. Kreyssig, Y.-Z. Zhang, H. O. Jeschke, R. Valenti, F. Yokaichiya, E. Colombier, J. Yan, T. C. Hansen, T. Chatterji, R. J. McQueeney, P. C. Canfield, A. I. Goldman, and D. N. Argyriou, Nat. Mater. **8**, 471 (2009).

[8] J. Paglione and R. L. Greene, Nat. Phys. **6**, 645 (2010).

[9] D. C. Johnston, Adv. Phys. **59**, 803 (2010).

[10] M. D. Johannes, I. I. Mazin, and D. S. Parker, Phys. Rev. B **82**, 024527 (2010).

[11] G. R. Stewart, Rev. Mod. Phys. **83**, 1589 (2011).

[12] M. D. Lumsden and A. D. Christianson, J. Phys.: Condens. Matter **22**, 203203 (2010).

[13] M. Gooch, B. Lv, K. Sasmal, J. H. Tapp, Z. J. Tang, A. M. Guloy, B. Lorenz, and C.-W. Chu, Physica C **470**, S276 (2010).

[14] H. S. Jeevan, Z. Hossain, D. Kasinathan, H. Rosner, C. Geibel, and P. Gegenwart, Phys. Rev. B **78**, 052502 (2008).

[15] A. I. Goldman, A. Kreyssig, K. Prokes, D. K. Pratt, D. N. Argyriou, J. W. Lynn, S. Nandi, S. A. J. Kimber, Y. Chen, Y. B. Lee, G. Samolyuk, J. B. Leao, S. J. Poulton, S. L. Bud'ko, N. Ni, P. C. Canfield, B. N. Harmon, and R. J. McQueeney, Phys. Rev. B **79**, 024513 (2009).

[16] W. O. Uhoya, J. M. Montgomery, G. M. Tsoi, Y. K. Vohra, M. A. McGuire, A. S. Sefat, B. C. Sales, and S. T. Weir, J. Phys.: Condens. Matt. **23**, 122201 (2011).

[17] R. Mittal, S. K. Mishra, S. L. Chaplot, S. V. Ovsyannikov, E. Greenberg, D. M. Trots, L. Dubrovinsky, Y. Su, T. Brueckel, S. Matsuishi, H. Hosono, and G. Garbarino, Phys. Rev. B **83**, 054503 (2011).

[18] J. R. Jeffries, N. P. Butch, K. Kirshenbaum, S. R. Saha, G. Samudrala, S. T. Weir, Y. K. Vohra, and J. Paglione, Phys. Rev. B **85**, 184501 (2012).

[19] S. R. Saha, N. P. Butch, T. Drye, J. Magill, S. Ziemak, K. Kirshenbaum, P. Y. Zavalij, J. W. Lynn, and J. Paglione, Phys. Rev. B **85**, 024525 (2012).

[20] A. S. Sefat, Rep. Prog. Phys. **74**, 124502 (2011).

[21] W. Yu, A. A. Aczel, T. J. Williams, S. L. Budko, N. Ni, P. C. Canfield, and G. M. Luke, Phys. Rev. B **79**, 020511(R) (2009).

[22] S. Kasahara, T. Shibauchi, K. Hashimoto, Y. Nakai, H. Ikeda, T. Terashima, and Y. Matsuda, Phys. Rev. B **83**, 060505(R) (2011).

[23] A. Kreyssig, M. A. Green, Y. Lee, G. D. Samolyuk, P. Zajdel, J. W. Lynn, S. L. Bud'ko, M. S. Torikachvili, N. Ni, S. Nandi, J. B. Leao, S. J. Poulton, D. N. Argyriou, B. N. Harmon, R. J. McQueeney, P. C. Canfield, and A. I. Goldman, Phys. Rev. B **78**, 184517 (2008).

[24] J. H. Soh, G. S. Tucker, D. K. Pratt, D. L. Abernathy, M. B. Stone, S. Ran, S. L. Bud'ko, P. C. Canfield, A. Kreyssig, R. J. McQueeney, and A. I. Goldman, Phys. Rev. Lett. **111**, 227002 (2013).

[25] H. Gretarsson, S. R. Saha, T. Drye, J. Paglione, J. Kim, D. Casa, T. Gog, W. Wu, S. R. Julian, and Y.-J. Kim, Phys. Rev. Lett. **110**, 047003 (2013).

[26] S. R. Saha, N. P. Butch, K. Kirshenbaum, J. Paglione, and P. Y. Zavalij, Phys. Rev. Lett. **103**, 037005 (2009).

[27] J.-F. Lin, V. V. Struzhkin, S. D. Jacobsen, M. Y. Hu, P. Chow, J. Kung, H. Liu, H.-K. Mao, and R. J. Hemley, Nature (London) **436**, 377 (2005).

[28] J.-P. Rueff and A. Shukla, Rev. Mod. Phys. **82**, 847 (2010).

[29] R. S. Kumar, Y. Zhang, Y. Xiao, J. Baker, A. Cornelius, S. Veeramalai, P. Chow, C. Chen, and Y. Zhao, Appl. Phys. Lett. **99**, 061913 (2011).

[30] G. Vankó, T. Neisius, G. Molnar, F. Renz, S. Karpati, A. Shukla, and F. M. F. de Groot, J. Phys. Chem. B **110**, 11647 (2006).

[31] H. Gretarsson, A. Lupascu, J. Kim, D. Casa, T. Gog, W. Wu, S. R. Julian, Z. J. Xu, J. S. Wen, G. D. Gu, R. H. Yuan, Z. G. Chen, N.-L. Wang, S. Khim, K. H. Kim, M. Ishikado, I. Jarrige, S. Shamoto, J.-H. Chu, I. R. Fisher, and Y.-J. Kim, Phys. Rev. B **84**, 100509(R) (2011).

[32] H. Kotegawa, T. Kawazoe, H. Sugawara, K. Murata, and H. Tou, J. Phys. Soc. Jpn. **78**, 083702 (2009).

[33] K. Matsubayashi, N. Katayama, K. Ohgushi, A. Yamada, K. Munakata, T. Matsumoto, and Y. Uwatoko, J. Phys. Soc. Jpn. **78**, 073706 (2009).

[34] K. Kirshenbaum, N. P. Butch, S. R. Saha, P. Y. Zavalij, B. G. Ueland, J. W. Lynn, and J. Paglione, Phys. Rev. B **86**, 060504(R) (2012).

[35] S. Speziale, A. Milner, V. E. Lee, S. M. Clark, M. P. Pasternak, and R. Jeanloz, Proc. Natl. Acad. Sci. U.S.A. **102**, 17918 (2005).

[36] L. Ortenzi, H. Gretarsson, S. Kasahara, Y. Matsuda, T. Shibauchi, K. D. Finkelstein, W. Wu, S. R. Julian, Y.-J. Kim, I. I. Mazin, and L. Boeri, arXiv:1408.4058.